JOURNAL OF Materials CHEMISTRY

Characterization of $La_{0.67}Ca_{0.33}MnO_{3\pm\delta}$ particles prepared by the sol–gel route

Carlos Vázquez-Vázquez,*[a] M. Carmen Blanco,[a] M. Arturo López-Quintela,[a] Rodolfo D. Sánchez,[b] José Rivas[b] and Saúl B. Oseroff[c]

[a]*Departamento de Química-Física, Universidade de Santiago de Compostela, E-15706, Santiago de Compostela, Spain*

[b]*Departamento de Física Aplicada, Universidade de Santiago de Compostela, E-15706, Santiago de Compostela, Spain*

[c]*Department of Physics, College of Sciences, San Diego State University, San Diego CA 92182, USA*

We report in this work the characterization of $La_{0.67}Ca_{0.33}MnO_{3\pm\delta}$ particles synthesized *via* sol–gel technology starting from an aqueous solution of the metallic nitrates and using urea as gelificant agent. The gelification is assumed to happen through the formation of polynuclear species by condensation reactions between hydroxo complexes. Gels were decomposed at 250 °C and calcined for 3 h at temperatures ranging from 300 to 1000 °C. Complete crystallization takes place at *ca.* 600 °C. The powders were structurally characterized by X-ray diffraction and their structural parameters were calculated using the Rietveld method. The Mn^{IV} content of the several samples was determined to be higher than the stoichiometric 33%. TEM micrographs show elongated particles of which the polar (long) axis size increases from 40 to 300 nm as the calcination temperature increases. Magnetization and magnetoresistance studies are reported showing that the particles smaller than 80 nm behave as single magnetic domains while the large ones behave as multidomains. A magnetoresistance of 12% at 1 kOe was observed for all the particles synthesized by this sol–gel method.

In the last four years much work has been published for thin films[1–4] and ceramic samples[5] of perovskite manganates, $R_{1-x}B_xMnO_{3\pm\delta}$ (R = La, Pr, Nd, Sm; B = Ca, Sr, Ba, Pb), showing giant magnetoresistance behaviour. The study of the giant magnetoresistance (GMR) in these materials has two main interests: (i) in basic science, in order to find a correct model to explain their magnetotransport properties, which is still now not well understood,[6–9] and (ii) their industrial applications (magnetic sensors, magnetic recording heads). However, all these studies were conducted at high magnetic fields (*ca.* 5 T) whereas most industrial applications use low magnetic fields.

The preparation methods used so far have several drawbacks: (i) quite thick films of $\geqslant$150 nm are produced, and grain sizes of the ceramic samples are of the order of microns; (ii) synthesis requires high temperatures and long periods of time; (iii) high costs of the devices needed for the thin film preparation; (iv) for ceramic samples, poor sintering behaviour, non-uniformity of particle size and shape, lack of reproducibility, multiphase character, and loss of stoichiometry due to volatilization of reactants at high temperatures.

The sol–gel process has a potential advantage over the other methods not only for achieving homogeneous mixing of the components on the atomic scale, but also for the possibility of forming films or fibers from gels which are of technological importance.[10,11] Other goals of the sol–gel route are lower processing temperatures and short annealing times, high purity of the materials, good control of the stoichiometry, size and shape of the particles, and particle sizes well below 100 nm at the lower processing temperatures.

In the present work we describe the synthesis of $La_{0.67}Ca_{0.33}MnO_{3\pm\delta}$ particles *via* sol–gel technology and calcination at several temperatures in order to study the effect of the calcination temperature on their structural, magnetic and magnetotransport properties.

Experimental

In the synthesis procedures carried out in this work all chemicals were used without further purification. All reagent-grade chemicals were provided by Aldrich (Steinheim, Germany), except $La(NO_3)_3\cdot 6H_2O$ which was provided by Fluka (Buchs, Switzerland). $La(NO_3)_3\cdot 6H_2O$ and La_2O_3 were dried in a vacuum desiccator and stored in an inert glove box before use since they are highly hygroscopic. $Mn(NO_3)_2\cdot 6H_2O$ was kept refrigerated, owing to its low melting point (*ca.* 25 °C), and handled in an inert glove box. In order to obtain a polycrystalline reference pattern, $La_{0.67}Ca_{0.33}MnO_{3\pm\delta}$ was synthesized by solid state reaction from stoichiometric amounts of La_2O_3, CaO and Mn_2O_3. This mixture was pelletized applying a pressure of 3.8×10^3 kg cm^{-2} and then annealed at 1200 °C in two steps for 24 and 72 h, and after at 1300 °C in two steps for 24 and 72 h, with intermediate grindings in an agate mortar after each step.

For the synthesis of $La_{0.67}Ca_{0.33}MnO_{3\pm\delta}$ *via* sol–gel technology, urea was used as the gelification agent. As starting materials, stoichiometric amounts of $La(NO_3)_3\cdot 6H_2O$, $Ca(NO_3)_2\cdot 4H_2O$ and $Mn(NO_3)_2\cdot 6H_2O$ were used owing to their high solubility in water. The initial concentrations were 0.134 M in La^{III}, 0.066 M in Ca^{II} and 0.2 M in Mn^{II} and the urea concentration was fixed at $\psi = 10$, with $\psi = [\text{urea}]/\{[La^{III}]+[Ca^{II}]+Mn^{II}]\}$. The reasons for using this value of ψ are given elsewhere.[12] The solvent was evaporated directly on a hot plate with continuous stirring at temperatures ranging between 75 and 137 °C, which corresponds to the melting point of urea. When cooling, a pink gel formed, which was decomposed in an oven at 250 °C in air for 3 h, yielding a fairly porous precursor. After milling in an agate mortar, the precursor was calcined for 3 h at several temperatures (ranging

* E-mail: qfmatcvv@usc.es

between 300 and 1000 °C) in order to study the effect of the particle size on their structural, magnetic and magnetotransport properties. Decomposition and calcination were carried out in a Quastar HEM-L-1 furnace in a static air atmosphere with a heating rate of *ca.* 10 °C min^{-1} up to the calcination temperature. All the samples were quenched in air to room temperature after calcination.

Values of pH were measured with a pH-meter Crison Digit 501 using a Radiometer GK2401C combined electrode with an Ag/AgCl system as internal reference. The structural characterization of the polycrystalline powders was carried out by X-ray powder diffraction, using a diffractometer Philips PW-1710 with Cu anode (Cu-Kα radiation $\lambda = 1.541\,86$ Å). The measurements were performed in air at room temperature. The oxygen content was determined by iodometric titrations of Mn^{III} and Mn^{IV}. Transmission electron microscopy was carried out with a Philips CM-12 working at 80 kV. IR spectroscopy measurements were carried out in a Bruker IFS 66V spectrophotometer. KBr pellets between rock salt plates were used and IR spectra were scanned between 4000 and 400 cm^{-1} with a scan resolution of 2 cm^{-1}. Thermogravimetry was carried out using a Perkin Elmer TGA 7 thermobalance. The experiments were carried out under N_2 at a heating rate of 10 °C min^{-1} up to 900 °C.

The magnetic properties of the samples were measured with a DMS 1660 vibrating sample magnetometer (VSM) between 100 and 300 K. Electrical resistivity, as a function of temperature and external magnetic field, was carried out with the standard dc four-probe method between 77 and 300 K; the powders were pressed at 6×10^3 kg cm^{-2} into disks of 13 mm diameter.

Electrochemical processes were carried out in 1 M KOH solution using a parallelepiped-shaped sample of $3 \times 2 \times 13$ mm^3 as working electrode. Four electrical contacts were established using silver paste, which was then separated from the electrolyte with silicon rubber. After electrochemical treatments the sample was washed with water and dried before the electrical measurements.The counter-electrode was a thin platinum wire of 0.35 mm diameter. A Crison cat. no. 52–40 Ag/AgCl electrode standardized with reference to NHE ($E^\circ = +207$ mV at 25 °C) served as the reference electrode. The oxidation was carried out under an anodic potential of +600 mV over 48 h and this sample was submitted afterwards to a reduction at −200 mV over 48 h.

Results and Discussion

Mechanism of gel formation

The role of the urea in the synthesis is very important.[12] In aqueous solution, metallic ions are coordinated by water molecules, but when an aqueous solution of urea is heated at temperatures $\geqslant 75$ °C the decomposition of urea to CO_3^{2-} and NH_3 (with release of hydroxide ions) becomes significant.[13] In the absence of acids the following reaction takes place:

$$\text{urea} \rightarrow NH_4^+ \; CNO^-$$

In acid media a rapid quantitative conversion of the cyanate ion to ammonium ion occurs:[14]

$$CNO^- + 2\,H^+ + 2\,H_2O \rightarrow NH_4^+ + H_2CO_3$$

The rate of decomposition depends on the temperature and urea concentration.[14] Some new ligands which can substitute water molecules in their coordination positions around the metal ions (NH_4^+, OH^-, CO_3^{2-}) appear in solution. The substitution degree of water by other ligands depends on the nature and concentration of metallic ions and ligands. The removal of water by evaporation promotes the substitution of water ligands, according to the following equation:

$$[M(H_2O)_m]^{n+} + xL^{q-} \rightarrow [M(H_2O)_{m-x} \cdot L_x]^{p+} + xH_2O$$

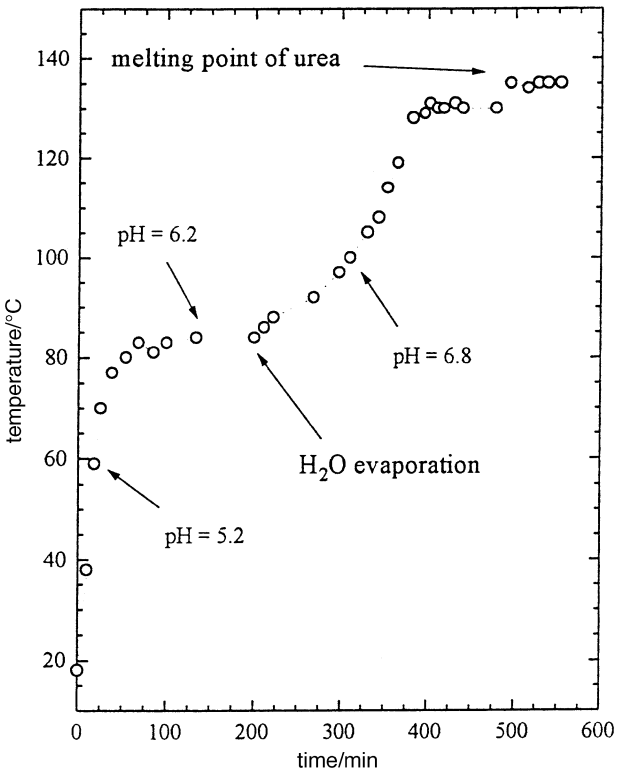

Fig. 1 Variation of the temperature and pH of the solution during the evaporation process

where M = La, Ca or Mn and L = NH_3, OH^-, CO_3^{2-} or urea. Urea ligands can coordinate metallic ions through the carbonyl or the amino group,[15] for Mn^{II} coordination occurs through the oxygen of urea.[16] It should be noted that the IR spectra of tetramethylurea (tmu) complexes of lanthanide elements, $[Ln(tmu)_6][ClO_4]_3$, indicate also the presence of O-coordination.[17]

The initial aqueous solution is slightly acidic pH (*ca.* 5.2). The pH remains acidic during most of the evaporation process, increasing a little as water removal proceeds owing to the decomposition of urea, and the solution reaches neutral pH values (Fig. 1). The small increase in pH is an indication that urea decomposes to only a small extent. This decomposition releases hydroxide ions which favours the hydrolysis of cations which leads to the formation of small amounts of a precipitate. The X-ray diffraction pattern of the dried precipitate indicates the presence of $La_2O(CO_3)_2 \cdot xH_2O$ ($x = 1$–2, JCPDS-ICDD Card No. 28–512) and, in lower percentages, of hexagonal $La(CO_3)OH$ (JCPDS-ICDD Card No. 26-815). We observe only lanthanum compounds in the precipitate due to the higher acidity of La^{III} ions compared to the other cations (Ca^{II}, Mn^{II}) present in solution.

For the hydrolysis reaction

$$[Mn(H_2O)_x]^{n+} \overset{K_1}{\longleftrightarrow} [Mn(H_2O)_{x-1}(OH)]^{(n-1)+} + H_{aq}^+$$

Sillén *et al.* have reported the hydrolysis constants for several metal ions at 25 °C.[18] La^{III} has a pK_1 ranging between 8.3 and 10.7; for Ca^{II}, $pK_1 = 13.4$, and for Mn^{II}, $pK_1 = 10.5$. Therefore, La^{III} ions show a higher tendency towards hydrolysis.

The presence of $La_2O(CO_3)_2 \cdot xH_2O$ in the precipitate leads us to consider the formation of polynuclear species by condensation reactions between the hydroxo complexes.[19] These polynuclear products are held together by hydroxo-, $[M(OH)(OH)M]^{2n+}$, or oxo-bridges: $[M-O-M]^{2n+}$.

When the mixture is sufficiently concentrated the temperature rises to the melting point of urea, around 137 °C.[20] The temperature increase leads to a larger extent of urea decompo-

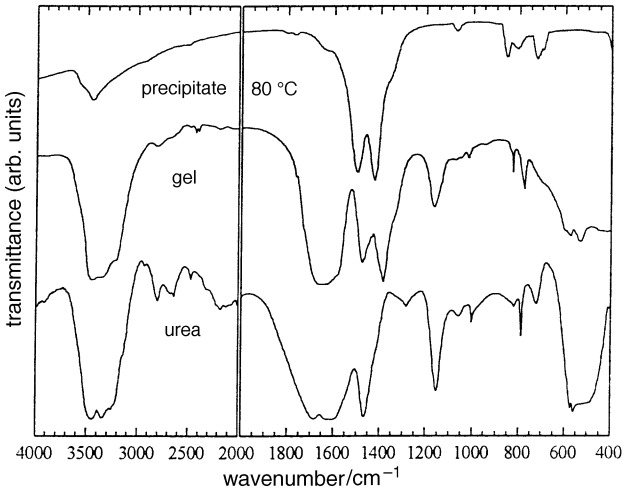

Fig. 2 IR spectra of the as-prepared gel and the precipitate formed at 80 °C, compared with commercial urea

Table 1 Main absorption maxima for urea and their assignments according to Penland *et al.*[15]

observed frequencies/cm^{-1}	vibration assignment
3457, 3349, 3260	N—H stretching
1682	C=O stretching and NH_2 bending
1607	NH_2 bending and C=O stretching
1467	out-of-phase C—N stretching
1154	in-plane NH_2 rocking
1004	in-phase C—N stretching
573, 559	N—C—O deformation
500	N—C—N deformation

sition raising the pH due to hydroxide release. The decomposition of urea is clearly indicated by the smell of ammonia and bubbles observed in the mixture.

At this stage the mixture is then cooled and a large increase in viscosity is observed leading to the formation of a gel. Metallic ions will be then located in the gel network with an statistical distribution according to the stoichiometric amounts of these ions in the starting solution.

The IR spectrum of this gel differs only slightly from commercial urea (Fig. 2). Table 1 lists absorption maxima for urea and assignments according to Penland *et al.*[15] The bands at 1384 and 825 cm^{-1} in the IR spectra of the gel are assigned to the nitrate group.

The shift of the C=O stretching to lower frequencies (1652 cm^{-1}) suggested the presence of hydrogen bonding inside the gel,[21] as a consequence of hydroxide ions. The band observed at *ca.* 1620–1600 cm^{-1} corresponds to the free NH_2 bending vibration. There are small shifts of other bands to higher frequencies: C—N stretching (1474 and 1017 cm^{-1}), NH_2 rocking (1164 cm^{-1}) and N—C—N deformation (531 cm^{-1}) that also indicates the formation of oxygen–metal bonds. This coordination increases the single bond character of the carbonyl group, increasing the importance of the resonance hybrids with higher double bond character of the C—N bonds.

The IR spectra of the precipitate dried at 80 °C is quite similar to that published by Aumont *et al.* for $La(OH)CO_3$ [22] and major absorptions are given in Table 2. This is in accord with the X-ray diffraction results because when $x=1$ the formula $La_2O(CO_3)_2 \cdot xH_2O$ can be considered as formed by two molecules of $La(OH)CO_3$. The differences observed with the data previously reported may be due to uncertainty in the water content.

Perovskite crystallization

$La_{0.67}Ca_{0.33}MnO_{3\pm\delta}$ crystallizes in a structure which shows an orthorhombic distortion with respect to the ideal cubic perovskite ABO_3, belonging to space group *Pbnm*.[23] In the perovskite structure, A cations are coordinated by twelve oxygen ions and B cations by six. The unit cell can be represented by A ions at the corners of a cube with B ions at the body center and oxygen ions at the center of the faces. The A cation is normally found to be somewhat larger than the B cation. In order to have contact between the A, B and O ions, R_A+R_O should be equal to $\sqrt{2}(R_B+R_O)$, where R_A, R_B and R_O are the ionic radii. Goldschmidt has shown that the perovskite structure is stable within tolerable limits of cations sizes.[24] He defines a tolerance factor, t, as $R_A+R_O=t\sqrt{2}(R_B+R_O)$. The perovskite structure occurs only within the range $0.75<t<1.00$; however, this is not a sufficient condition, since A and B cations must, in themselves, be stable in twelve- and six-coordination, respectively. In oxides, the bounds for the cationic radii are $r_A>0.90$ Å and $r_B>0.51$ Å.[24]

If $0.75<t<0.9$, a cooperative buckling of corner-shared octahedra to optimize the A—O bond lengths enlarges the unit cell and produces an orthorhombic distortion of the unit cell, containing four formula units. This buckling of the corner-shared octahedra decreases the cation–anion–cation angle ϕ from 180°.[25] This distortion is common in all ABO_3 perovskites, with creation of 'free space' in the structure by small lanthanide atoms or by substitution of larger ones by smaller alkali or alkaline earth atoms. This is the so called O-type structure, with $a\leqslant c/\sqrt{2}\leqslant b$ for orthorhombic *Pbnm* perovskites.

We must consider another distortion, related to the strong Jahn–Teller character of Mn^{III} in the octahedral sites, due to its $3d^4$ $t_{2g}{}^3e_g{}^1$ electron configuration. This distortion does not change the lattice symmetry (*Pbnm*) but modifies the cell deformation in such a way that $c/\sqrt{2}\leqslant a\leqslant b$ (O′-type structure). The Jahn–Teller split of the e_g band is progressively reduced as the Ca^{II} concentration increases in the intermediate $La_{1-x}Ca_xMnO_3$ compounds due to the conversion of Mn^{III} to Mn^{IV}; *i.e.* from $3d^4$ ($t_{2g}{}^3e_g{}^1$) to $3d^3$ ($t_{2g}{}^3e_g{}^0$) electron configuration, respectively.[26]

For the sol–gel technology samples it is observed that $La_{0.67}Ca_{0.33}MnO_{3\pm\delta}$ shows an incipient crystallization at 500 °C and complete crystallization takes place at *ca.* 600 °C. Below this temperature we observe very small peaks of calcite (rhombohedral $CaCO_3$, JCPDS-ICDD Card No. 5-586). The results obtained as a function of the calcination temperature are shown in Fig. 3.

Table 2 Observed main absorption maxima of the precipitate formed at 80 °C, compared with those reported by Aumont *et al.* for $La(CO_3)OH$[22]

observed frequencies/cm^{-1}	$La(CO_3)OH$ frequencies/cm^{-1}	vibration assignment
1069	1085, 1100	ν_1 ($CO_3{}^{2-}$)
855, 808	875	ν_2 ($CO_3{}^{2-}$)
1498, 1423	1515–1480, 1460–1440, 1420–1410	ν_3 ($CO_3{}^{2-}$)
722, 698	725, 695	ν_4 ($CO_3{}^{2-}$)
3580	3625, 3640	ν_{s1} (OH^-)
3452	3470, 3475, 3487, 3495	ν_{s2} (OH^-)

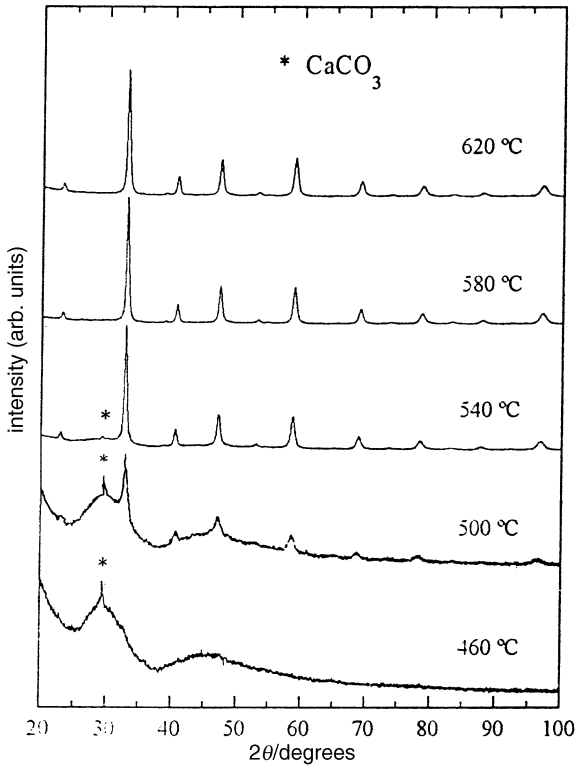

Fig. 3 X-Ray diffraction patterns of $La_{0.67}Ca_{0.33}MnO_{3\pm\delta}$ samples as a function of the calcination temperature. All the samples were calcined 3 h at each temperature. Crystallization is complete at *ca.* 600 °C.

In order to obtain more details about the nature of the samples below the crystallization temperature, they have been studied by IR spectroscopy and thermogravimetry.

IR spectra of the precursor calcined at 250 °C and subsequent treatments of this sample are presented in Fig. 4. At 250 and 300 °C the IR spectra show several differences with respect to the spectrum of the gel. The broad bands at *ca.* 3385 and 1630 cm^{-1} indicate that amine and carbonyl groups are still present, while the bands at 1481 and 559 cm^{-1} indicate the existence of C—N stretching and N—C—O deformation, respectively. However, some new bands arise. The band at 1734 cm^{-1} is due to free carbonyl vibration, and indicates the formation of a coordinate bond between the N and the central metal atom, as was observed by Penland *et al.* for palladium(II) and platinum(II) complexes with urea.[15] The formation of the N→M bond increases the electron demand by the donor nitrogen atom and blocks the resonance between this nitrogen

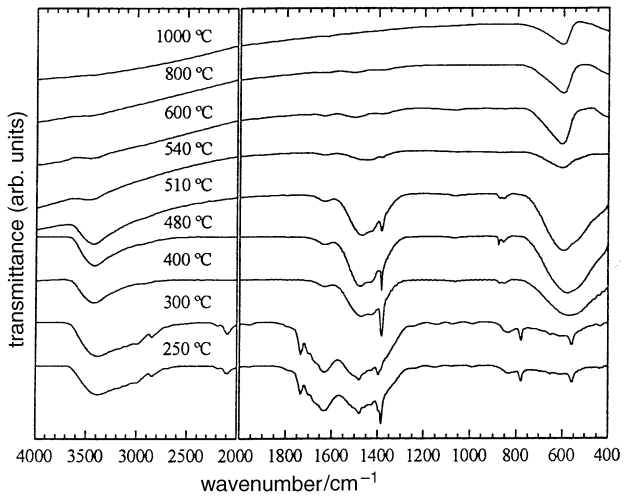

Fig. 4 IR spectra evolution as a function of the calcination temperature

atom and the carbonyl group, increasing the C=O double bond character.

Penland *et al.* have also observed for these urea complexes of Pd^{II} and Pt^{II} two additional bands in the high-frequency region, at lower frequencies than the N—H stretching vibrations. They have assigned these bands to the N—H stretching vibrations of the coordinated NH_2 group and concluded that only one nitrogen atom of each urea molecule coordinates to the central metal ion since both free and coordinated N—H frequencies were observed in the spectra.[15] This N-coordination can explain the broadening of the N—H stretching band to lower frequencies.

The bands at 1384 and 833 cm^{-1} arise from the presence of the nitrate group and they remain up to 540 °C. Below the perovskite crystallization, two bands are observed at *ca.* 1475 and 1430 cm^{-1} that can be assigned to the carbonate group.

This substantial change in the properties of the system when the perovskite crystallizes is accompanied with a loss of mass, as shown in Fig. 5. The sample calcined at 300 °C shows an initial small mass loss below 250 °C due to loss of water and a much larger mass loss above 400 °C that extends up to 850 °C. This second mass loss is related to carbonate and oxycarbonate decomposition as well as that of other secondary phases remaining from the urea decomposition.

Owing to the fact that each sample is calcined for 3 h at the corresponding calcination temperature, the decomposition is more complete at each temperature than in the thermograms, shifting the thermogravimetric curve to lower temperatures.

Structural and microstructural parameters were extracted from the X-ray data using the program LS1, based on the Rietveld method[27,28] and written in Microsoft Professional BASIC 7.0 by Lutterotti *et al.*[29] This program employs the Levenberg–Marquardt least-squares method to minimize the weighted sum of squared residuals:[30]

$$SSQ = \sum_i w_i(I_{i,exp} - I_{i,calc})^2$$

Peak profiles were modelled by pseudo-Voigt functions cor-

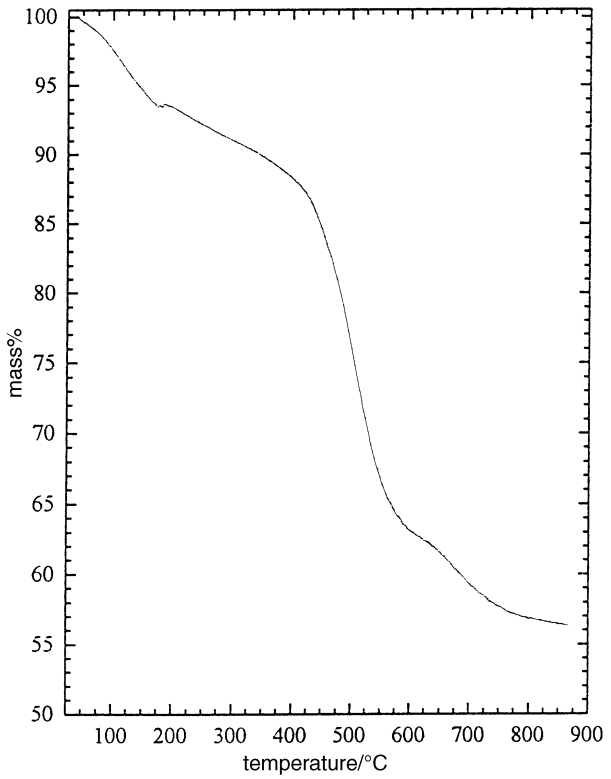

Fig. 5 Thermogram of the sample calcined for 3 h at 300 °C at a heating rate of 10 °C min^{-1}

rected for instrumental asymmetry. The background is reproduced by a polynomial expression and, if amorphous phase halos are present in the diffraction pattern, they are modelled inserting very broad Gaussians. The correction for preferred orientation is introduced following the March–Dollase model and proposed by Will *et al.*[31] The peak width, reproduced by the Caglioti equation,[32] the gaussianity of pseudo-Voigt function and two parameters for the asymmetry have to be fixed once a standard profile has been refined. In our case, the standard was a ceramic sample of $La_{0.67}Ca_{0.33}MnO_3$. This procedure is necessary in order to refine the microstructure, *i.e.* crystallite size and microstrain.

Besides small particle size, several crystal imperfections contribute to break the crystal into smaller incoherent diffracting domains as, for example, dislocation arrays, stacking faults or twins. Dislocations, vacancies, interstitials and substitutions manifest themselves through lattice microstrain. Because the Caglioti formula cannot reproduce all these possible broadening effects,[33] the authors have developed a model to connect profile width and shape directly to crystallite size (column length) and microstrain, along the various crystallographic directions, using conditions on cosine Fourier coefficients and their derivatives.[33,34]

X-Ray data were collected in the 2θ range 20–100° (12–100° for samples calcined below 600 °C) with a step interval of 0.02° and a time step of 10 s.

Results are presented in Tables 3 and 4. Rietveld fits to the data for three representative calcination temperatures (520, 600 and 1000 °C) are shown in Fig. 6. Rietveld fits for samples prepared at temperatures below *ca.* 580 °C can be subject to additional errors such as small changes in perovskite stoichiometry because of the presence of amorphous phase halos and calcite, $CaCO_3$, as a secondary phase. As a consequence, the results for the samples in the range 500–580 °C should be interpreted with care because of the assumption of La-substitution by 1/3 of Ca atoms.

Lattice parameters, unit cell volumes and densities for the various samples are shown in Fig. 7. Below 600 °C we observe a decrease of all lattice parameters up to 530 °C and in the range 530–600 °C they remain almost constant. The initial decrease is due to calcium segregation as calcite, so the material does not have the correct stoichiometry of 67% La : 33% Ca but a higher percentage of La^{III} ions which are larger than Ca^{II} ions (1.15 and 1.05 Å for octahedral coordination, respectively).[35] For well crystallized samples, a significant increase of all parameters with the calcination temperature is observed

Table 3 Structural parameters for samples near the crystallization region. At low temperatures results are subjected to higher errors. Mass contents of calcite, $CaCO_3$, are specified. Some error factors are indicated at the bottom. Reflection (1 2 1) of the space group *Pbnm* is considered as preferred orientation (P.O.) $\Theta_{octahedra}$ represents the tilt angle between two octahedra

T/°C	500	520	540	560	580
a/Å	5.459(7)	5.454(6)	5.4491(1)	5.4496(5)	5.4495(5)
b/Å	5.486(5)	5.455(7)	5.4815(1)	5.4780(4)	5.4785(5)
c/Å	7.780(6)	7.744(4)	7.6896(4)	7.6908(6)	7.6896(7)
structure type	O	O	O′	O′	O′
x (La,Ca)	0.523(2)	0.486(2)	0.516(2)	0.5161(2)	0.5169(3)
y (La,Ca)	0.0005(35)	0.002(4)	0.0008(65)	0.00005(27)	0.002(1)
x [O(1)]	−0.02(1)	−0.224(5)	0.010(5)	−0.003(2)	−0.003(2)
y [O(1)]	−0.000004(963)	0.03(2)	0.062(2)	0.075(2)	−0.058(4)
x [O(2)]	0.301(8)	0.27(2)	0.277(2)	0.276(3)	0.272(3)
y [O(2)]	0.156(7)	0.22(2)	0.208(3)	0.222(3)	0.217(2)
z [O(2)]	−0.0002(17)	0.007(11)	−0.0205(4)	−0.023(1)	0.028(2)
$\Theta_{octahedra}$/degrees	174.2	115.0	159.7	155.9	161.2
B_{iso}/Å^2	1.28(9)	1.07(2)	0.880(4)	0.92(1)	0.37(2)
P.O.(121)	—	1.06(5)	1.000(3)	0.992(4)	1.040(6)
%(m/m) $CaCO_3$	7.0	4.6	1.3	0	0
SSQ	4422.6	5852.8	5109.4	7080.8	9036.9
GOF	1.05	1.11	1.13	1.22	1.51
R_B (%)	4.38	15.1	3.80	8.54	4.13
R_{wp} (%)	5.09	5.89	5.34	6.65	8.08

Table 4 Structural parameters for crystallized samples as a function of calcination temperature. Error factors are specified at the bottom. Reflection (1 2 1) of the space group *Pbnm* is considered as preferred orientation. $\Theta_{octahedra}$ represents the tilt angle between two octahedra

T/°C	600	700	800	900	1000	ceramic
a/Å	5.4492(7)	5.4627(4)	5.4618(4)	5.4614(2)	5.4602(1)	5.46219(7)
b/Å	5.4767(7)	5.4821(5)	5.4788(3)	5.4783(1)	5.4769(1)	5.47685(6)
c/Å	7.6936(9)	7.7129(6)	7.7160(5)	7.7154(2)	7.7153(2)	7.71934(9)
structure type	O′	O′	O′	O′	O′	O′
x (La,Ca)	0.5139(5)	0.5159(2)	0.5175(2)	0.5178(2)	0.5184(1)	0.5200(1)
y (La,Ca)	0.002(2)	0.0005(8)	0.002(1)	0.0015(7)	0.0022(4)	0.0036(3)
x [O(1)]	−0.002(3)	−0.011(2)	−0.011(2)	−0.010(2)	−0.010(1)	−0.0056(8)
y [O(1)]	−0.075(5)	−0.074(3)	−0.066(3)	−0.072(2)	−0.069(2)	−0.062(1)
x [O(2)]	0.262(5)	0.278(2)	0.263(3)	0.282(2)	0.278(1)	0.275(1)
y [O(2)]	0.216(3)	0.234(2)	0.207(2)	0.231(2)	0.229(2)	0.222(1)
z [O(2)]	0.030(2)	0.028(1)	0.029(2)	0.032(1)	0.0309(8)	0.0317(7)
$\Theta_{octahedra}$/degrees	155.9	156.0	158.5	156.7	157.6	160.0
B_{iso}/Å^2	1.76(2)	0.47(1)	0.93(2)	1.11(1)	0.65(1)	0.032(13)
P.O.(121)	0.981(6)	0.986(4)	0.986(5)	0.963(3)	0.975(3)	0.945(3)
SSQ	8538.7	7306.7	6672.1	5914.2	7853.6	7591.1
GOF	1.46	1.35	1.29	1.22	1.40	1.38
R_B (%)	4.02	3.35	3.18	2.86	2.79	2.97
R_{wp} (%)	5.76	7.65	5.65	4.81	7.01	7.97

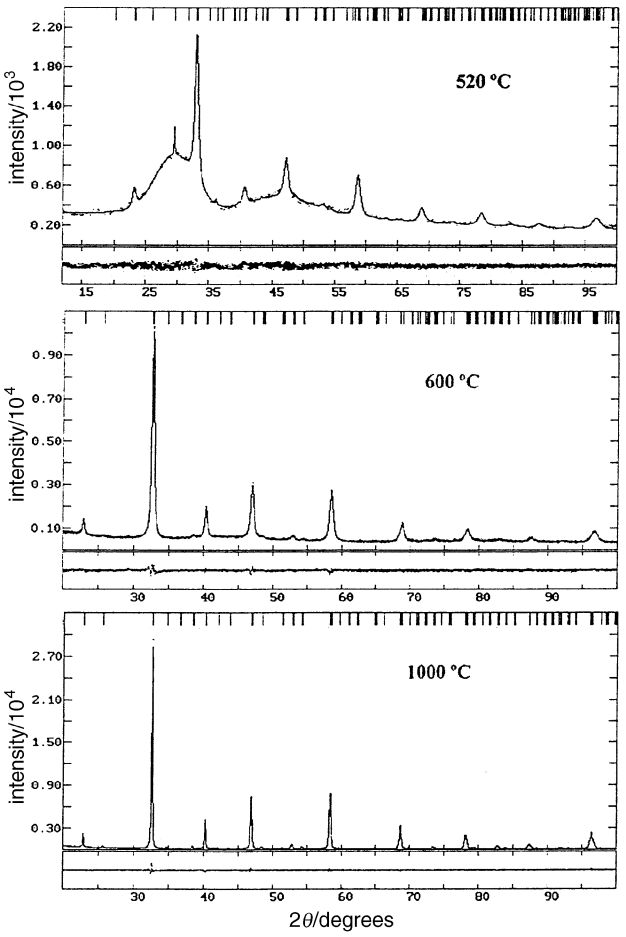

Fig. 6 Rietveld fits of samples prepared at 520, 600 and 1000 °C. Allowed reflections of the space group *Pbnm* are indicated at the top of graphics and the residuals at the bottom. For the sample prepared at 520 °C amorphous phase halos and additional reflections due to the rhombohedral calcite, $CaCO_3$ are observed.

between 600 and 700 °C and above this temperature a slow decrease is seen. This slow decrease of the unit cell volume above 700 °C is due to better compaction of the structure, leading to a higher density.

The orthorhombic deformation can be calculated by the formula[36]

$$D=\frac{1}{3}\sum_{i=1}^{3}\left|\frac{a_i-\bar{a}}{a}\right|100$$

where $a_1=a$, $a_2=b$, $a_3=c/\sqrt{2}$ and $\bar{a}=abc/\sqrt{2}$. This is a measurement of the distortions of the structure with respect to the ideal cubic perovskite structure, where all three lattice parameters are equivalent and, therefore, no distortion is seen. It is observed that D decreases rapidly as the calcination temperature increases, and almost vanishes at high temperatures (Fig. 8).

We have assumed an isotropic model for crystallite sizes and microstrains and results are shown in Fig. 9. As expected, an increase in the calcination temperature implies a growth of the crystallites, lowering at the same time microstrain effects because of better crystallinity of the samples.

We have no clear explanation for the sharp increase of lattice parameters between 600 and 700 °C but there are several factors which can affect the lattice parameters.

(*a*) The Mn^{IV} content present in the samples: Mn^{IV} has a smaller effective ionic radius than Mn^{III} (0.60 Å *cf.* 0.66 Å) in octahedral coordination.[35] The Mn^{IV} content was determined by iodometry (see below). The presence of smaller Mn^{IV} cations leads to a higher distortion of the perovskite structure, bending the Mn—O—Mn angle from the ideal perovskite value of 180°. Nevertheless, no clear tendency is observed in the angle between octahedra determined by the Rietveld method as a function of the calcination temperature (Tables 3 and 4).

(*b*) The size of the crystallite domains: small sizes can originate stresses in the structure which disappear when the structure is formed at higher temperatures.

(*c*) The presence of defects: all the orthorhombic perovskites show twinning, breaking the crystallite domains in smaller units. The presence of twins increases the stresses in the structure; *i.e.* increases the microstrain. At higher temperatures the energy supplied to the structure can be sufficient to anneal the structure and lower the microstrains.

(*d*) Changes in stoichiometry: the presence of vacancies in cationic positions can also strongly affect the lattice parameters; however, no segregation of secondary phases was observed by X-ray diffraction and the Rietveld method fits the experimental data fairly well.

Iodometry

In order to calculate the percentage of Mn^{IV} present in the samples iodometric titrations were carried out. The iodometry method used is based on that described by Vogel.[37] For this purpose, three assumptions were made: (*i*) La and Ca maintain the initial stoichiometric ratio 2:1; (*ii*) La and Ca have oxidation states of +3 and +2, respectively; and (*iii*) Mn can be present in oxidation states of +3 and +4.

A weighed amount of $La_{0.67}Ca_{0.33}MnO_{3\pm\delta}$ powders was dissolved in a stirred mixture of 10 ml of a 10 mass% KI aqueous solution and 2.5 ml 2 M HCl. Chlorine is produced by the reactions

$$2\ Mn^{III}+2\ Cl^-\rightarrow Cl_2+2\ Mn^{II}$$

$$Mn^{IV}+2\ Cl^-\rightarrow Cl_2+Mn^{II}$$

The *in situ* generated chlorine reacts with the iodide and iodine is formed:

$$Cl_2+2\ I^-\rightarrow 2\ Cl^-+I_2$$

This iodine is titrated with a standard volumetric solution of sodium thiosulfate (0.0202 N) until a clear and colorless solution is obtained. When the end-point is approached, three drops of 1 mass% starch solution are added in order to observe the colour change better.

$$2\ S_2O_3^{2-}+I_2\rightarrow 2\ I^-+S_4O_6^{2-}$$

Under the three former assumptions, the formula for the lanthanum manganate(III/IV) can be calculated: $La^{III}_{0.67}Ca^{II}_{0.33}Mn^{III}_{1-\alpha}Mn^{IV}_{\alpha}O_{3\pm\delta}$, where $3\pm\delta=(17+3\alpha)/6$.

As the analysis determines oxidation equivalents, the possibility of disproportionation of Mn^{III} to Mn^{II} and Mn^{IV} has to be considered:

$$2\ Mn^{III}\rightarrow Mn^{II}+Mn^{IV}$$

The Mn^{III} and Mn^{IV} content can be calculated from the titration results:

$$\text{mol } I_2=0.5\text{ mol } Mn^{III}+\text{mol } Mn^{IV}=[(1-\alpha)/2]\text{ mol } Mn^{III}+\alpha\text{ mol } Mn^{IV}$$

$$\text{giving } \alpha=\frac{m-206.235NV}{8NV-m}$$

where m is the mass of the sample and N and V are the normality and added volume of the $S_2O_3^{2-}$ standard volumetric solution.

Results are shown in Fig. 10. The Mn^{IV} content decreases rapidly to the theoretical value of 33% (1/3 Ca substitution) as the calcination temperature increases, so the oxygen content decreases close to 3.00.

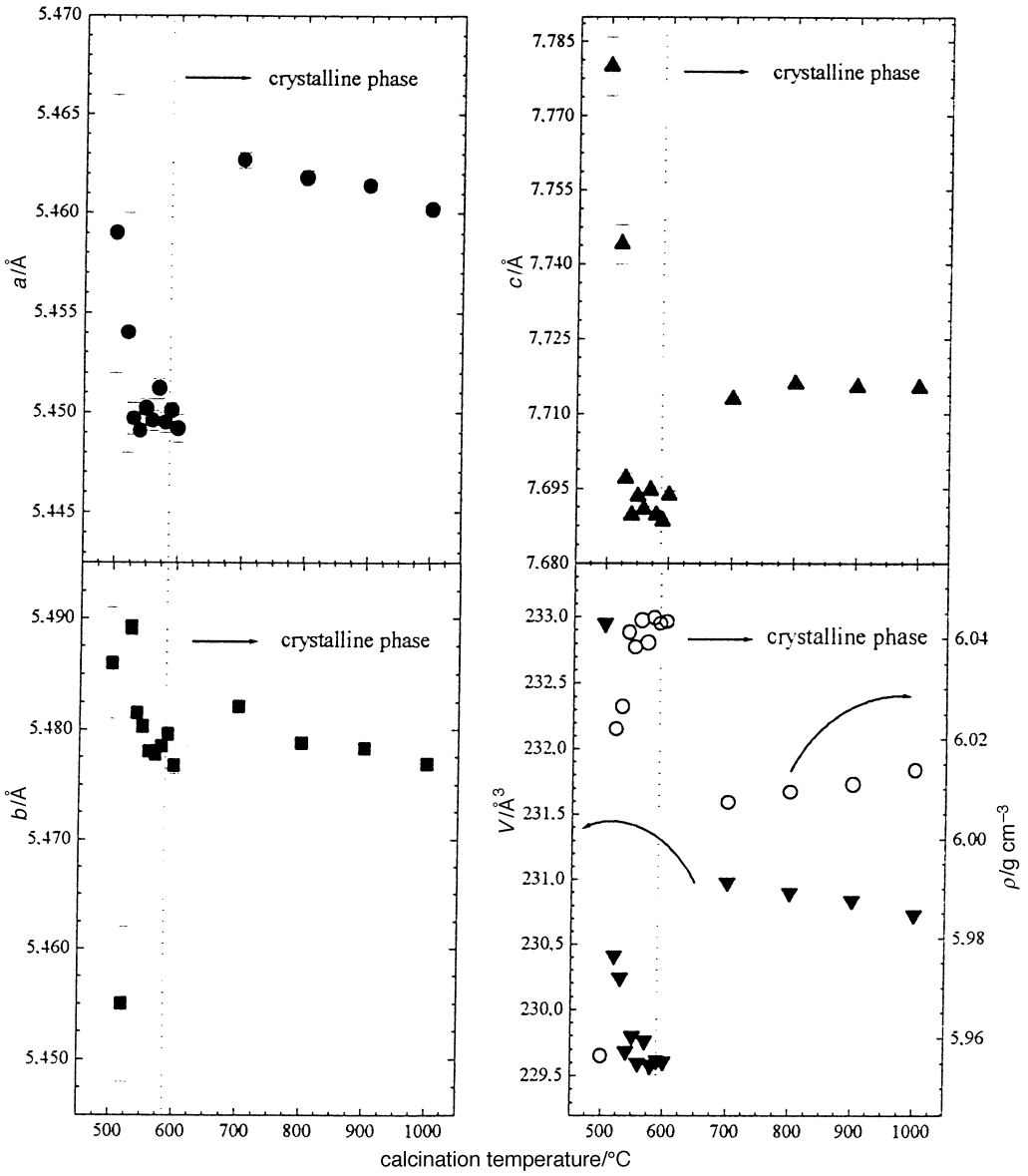

Fig. 7 Unit cell parameters, volume and density of the sol–gel samples as a function of the calcination temperature

This decrease of Mn^{IV} content acts in the opposite way to the unit cell volume tendency, which decreases above 700 °C, but it could explain to some extent the unit cell volume increase observed between 600 and 700 °C.

The best explanation for the lattice parameters jump between 600 and 700 °C seems to be the small size of the crystallite domains, which causes stresses in the structure. However, a more detailed structure study with powerful techniques (neutron diffraction) is needed in order to determine the presence of vacancies and the Mn^{IV} content, which is directly related to the magnetic structure.

Transmission electron microscopy

Fig. 11 shows several micrographs of sol–gel samples of $La_{0.67}Ca_{0.33}MnO_{3\pm\delta}$ synthesized at 540, 600, 800 and 1000 °C. At 540 °C we observe some material which has not yet crystallized, however, when the calcination temperature is increased to 600 °C only crystallized particles are obtained. Further increases on the calcination temperature imply a growth of the particles. TEM micrographs show elongated particles whose polar (long) axis size increases from 40 to 300 nm as the calcination temperature is increased. The TEM sizes are several times larger than those calculated by X-ray diffraction (Fig. 12). This can be understood if we take into account that one particle may consist of several crystallization domains[38] which is what is observed by X-rays while with TEM the whole particle is observed. Twinning and other structure defects (vacancies, dislocations) can explain the presence of the crystallite domains in the particle.

Magnetic properties

Hysteresis loops of the sol–gel samples prepared were measured between 100 and 300 K. Fig. 13 shows the coercive field of the samples as a function of temperature. We can see two behaviour types: for the larger particles (above an average particle size of *ca.* 80 nm) the coercive field drops continuously up to the bulk Curie point, $T_C = 265$ K, and paramagnetic behaviour is observed above this critical temperature; in the case of the smaller particles (below an average particle size of *ca.* 50 nm), superparamagnetic behaviour is observed below T_C, between 230 and 265 K. These results led us to consider the smaller particles as single domains, while the larger ones behave as usual ferromagnetic multidomains. Using a theoretical relation we have determined the critical size of spherical grains below which they are single domains.[39] The critical size was 80 nm, which is in good agreement with our experimental results.

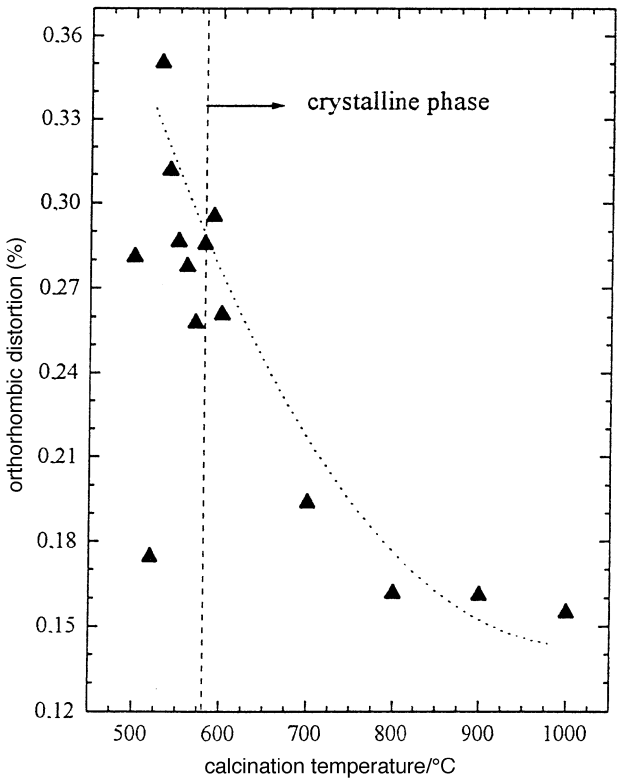

Fig. 8 Orthorhombic distortion of the different sol–gel samples compared with the ideal cubic perovskite structure ($D=0\%$). The dotted line is a guide to the eye.

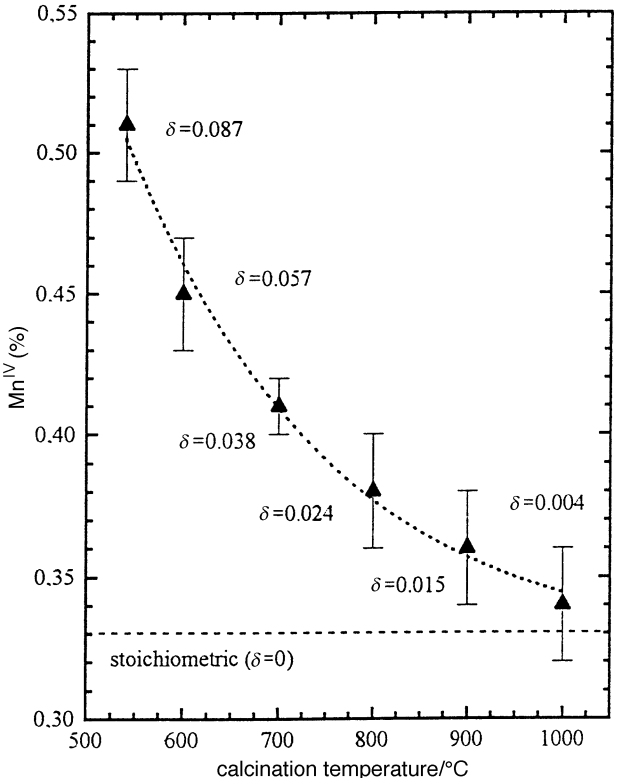

Fig. 10 Manganese(IV) content of the sol–gel samples, determined by iodometric titrations. The dotted line is a guide to the eye.

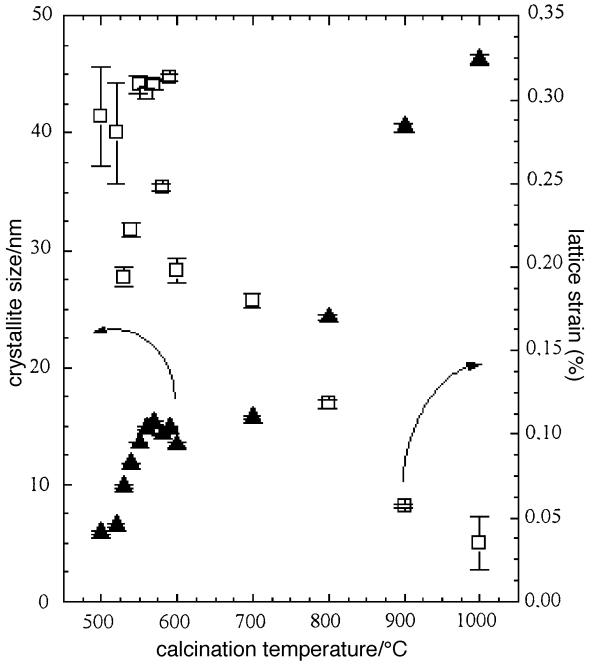

Fig. 9 Dependence of the crystallite size and lattice microstrain on the calcination temperature

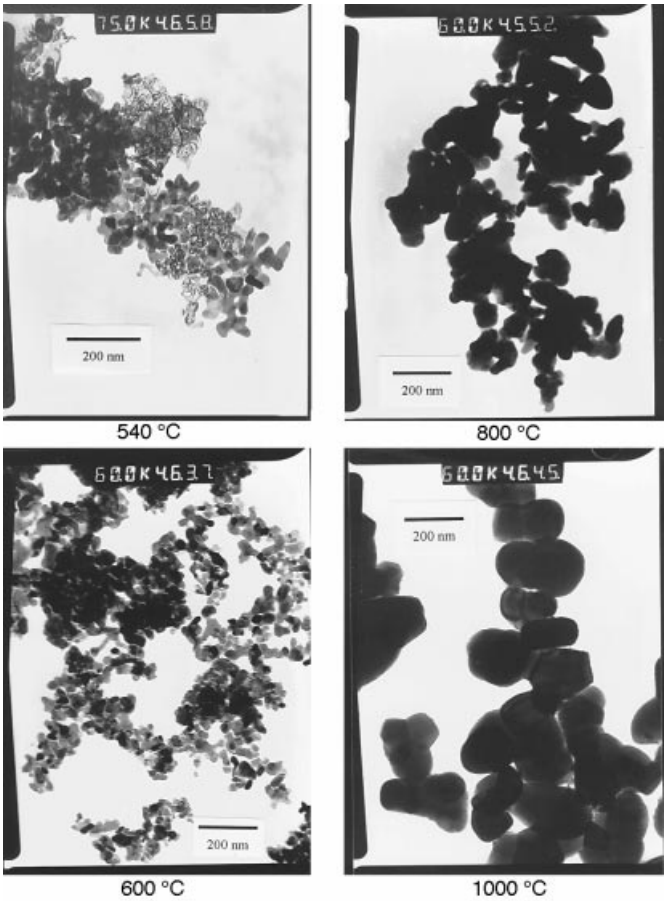

Fig. 11 Transmission electron micrographs of samples calcined for 3 h at 540, 600, 800 and 1000 °C. In all cases, the bar represents 200 nm.

Transport properties

The electrical resistivity, ρ, normalized by the value measured at 300 K, is observed to decrease as the particle size increases and the maximum of the resistivity shifts to higher temperatures as the particles becomes larger.[39,40] This shift can be primarily attributed to a change in the oxygen content as we shall show below in the electrochemically modified samples.

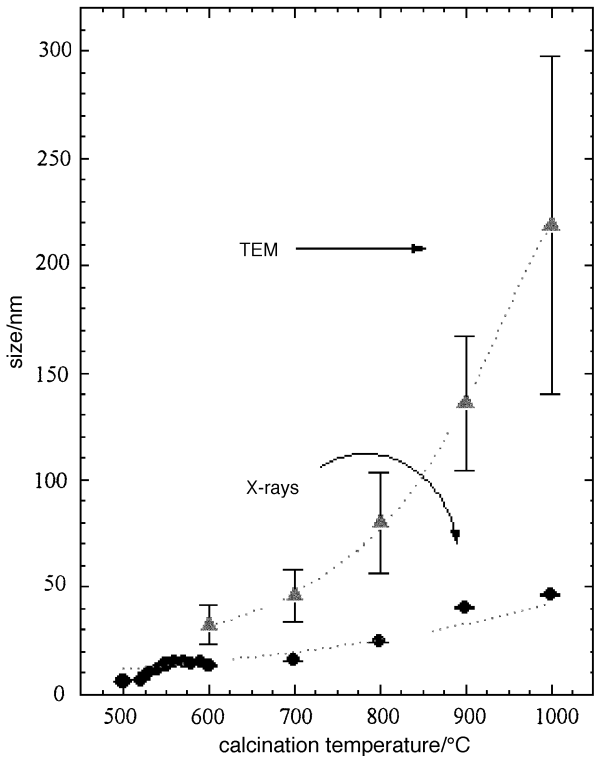

Fig. 12 Comparison of sizes obtained by X-ray diffraction, using the Rietveld method, and by transmission electron microscopy. The dotted lines are a guide to the eye.

The particle size has also a great influence in the magnetoresistance, $\Delta R/R_0=[(R_H-R_0)]/R_0$. Fig. 14 compares the magnetoresistance of the ceramic sample and a sol–gel sample synthesized at 700 °C. At 1 kOe, the ceramic sample shows a MR change of 5% *cf.* 12% for the sol–gel sample.[39]

This sol–gel sample was subjected to electrochemical processes which can modify the oxygen content at room temperature without any size increase, as in the conventional oxidation/reduction processes at high temperatures in controlled atmospheres. It is observed that oxidation of the sample shifts the maximum of the resistance to lower temperatures, while reduction shifts the maximum to higher temperatures (Fig. 15). The shift to lower temperatures for the oxidized sample is quite surprising because when a sample is oxidized in an O_2 atmosphere at high temperatures the opposite behaviour is observed.[5] As yet, we have no explanation for this behaviour but we have to take into account that our samples are not fully oxidized. However, these are only preliminary results and further work is in progress in order to understand this peculiar phenomenon.

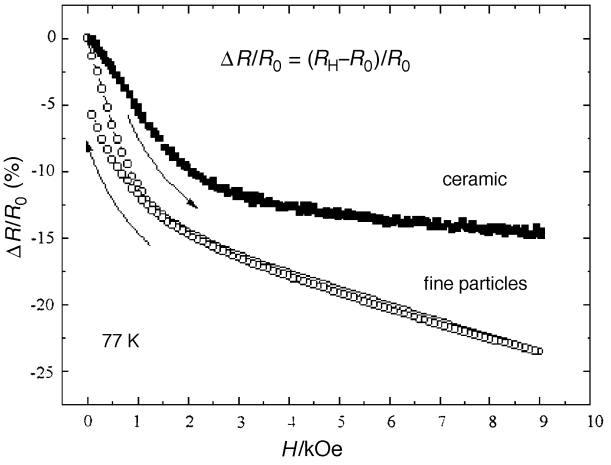

Fig. 14 Magnetoresistance at 77 K of fine particles of $La_{0.67}Ca_{0.33}MnO_{3\pm\delta}$ synthesized at 700 °C compared with the solid state reaction sample

The authors wish to acknowledge financial support from DGICYT-PB94-1528 (Spain) and NSF-DMR-91172122 (USA), and Dr. Senén Paz-Abuín for thermogravimetric measurements. C.V.V. also thanks Xunta de Galicia for financial support.

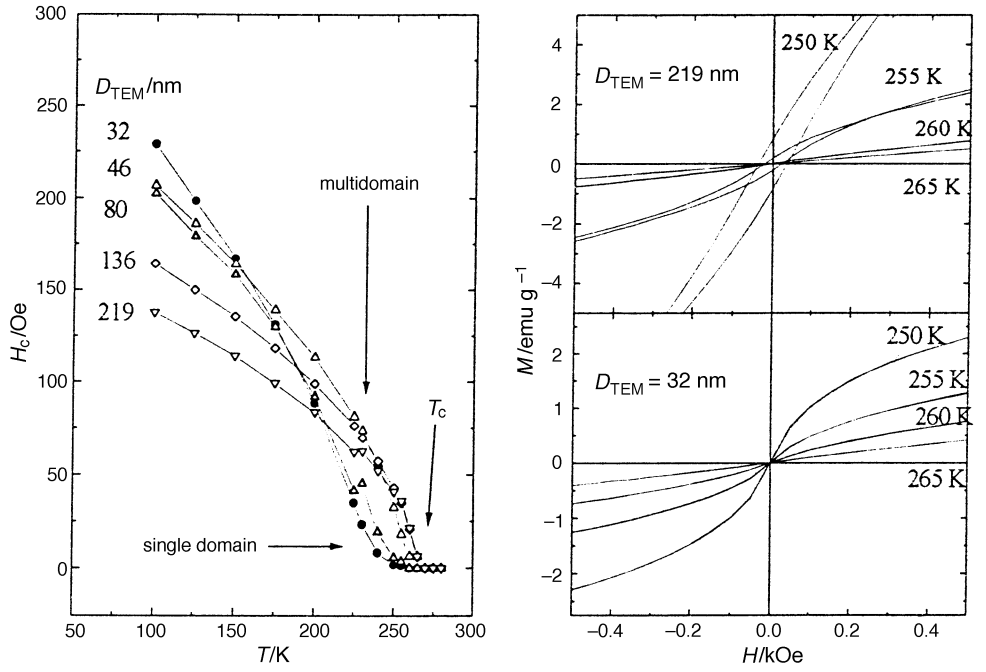

Fig. 13 Coercive fields of the sol–gel samples measured between 100 and 300 K, obtained from the hysteresis loops. Each sample is labelled after the average particle size obtained by transmission electron microscopy.

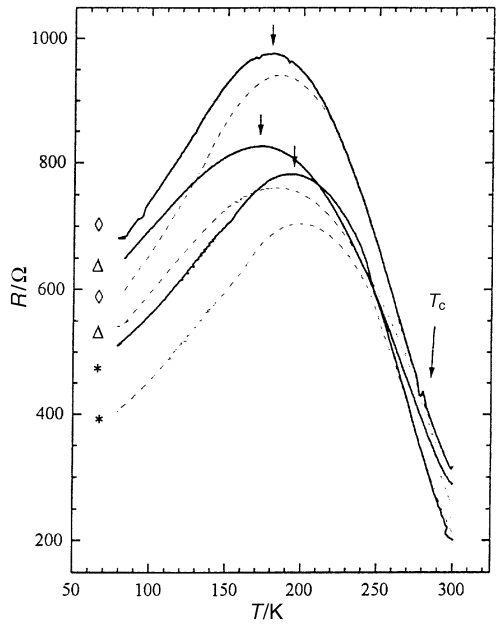

Fig. 15 Electrical resistance of $La_{0.67}Ca_{0.33}MnO_{3\pm\delta}$ fine particles prepared at 700 °C as a function of the temperature and at two different external magnetic fields (0 Oe, solid lines; 5 kOe, dashed lines). (✳), as-prepared particles; (△), after electrochemical oxidation of the as-prepared sample (48 h at $E=0.6$ V); and (◇), after electrochemical reduction of the previously oxidized sample (48 h at $E=-0.2$ V).

References

1 R. von Helmot, J. Wecker, B. Holzapfel, L. Schultz and K. Samwer, *Phys. Rev. Lett*., 1993, **71**, 2331.
2 K. Chahara, T. Ohno, M. Kasai and Y. Kozono, *Appl. Phys. Lett*., 1993, **63**, 1990.
3 S. Jin, T. H. Tiefel, M. McCormack, R. A. Fastnacht, R. Ramesh and L. H. Chen, *Science*, 1994, **264**, 413.
4 H. L. Ju, C. Kwon, Qi Li, R. L. Greene and T. Venkatesan, *Appl. Phys. Lett*., 1994, **65**, 2108.
5 H. L. Ju, J. Gopalakrishnan, J. L. Peng, G. C. Xiong, T. Venkatesan and R. L. Greene, *Phys. Rev. B*, 1995, **51**, 6143.
6 P. G. de Gennes, *Phys. Rev. B*, 1960, **118**, 141.
7 N. Furukawa, *J. Phys. Soc. Jpn*., 1994, **63**, 3214.
8 J. Inoue and S. Maekawa, *Phys. Rev. Lett*., 1995, **74**, 3407.
9 A. J Millis, P. B. Littlewood and B. I. Shraiman, *Phys. Rev. Lett*., 1995, **74**, 5144.
10 J. Livage, M. Henry and C. Sánchez, *Prog. Solid State Chem*., 1988, **18**, 259.
11 M. Kakihana, *J. Sol–Gel Sci. Technol*., 1996, **6**, 7.
12 J. Mahía, C. Vázquez-Vázquez, M. I. Basadre-Pampín, J. Mira, J. Rivas, M. A. López-Quintela and S. B. Oseroff, *J. Am. Ceram. Soc*., 1996, **79**, 407.
13 E. Matijevic and W. P. Hsu, *J. Colloid Interface Sci*., 1987, **118**, 506.
14 W. H. R. Shaw and J. J. Bordeaux, *J. Am. Chem. Soc*., 1955, **77**, 4729.
15 R. B. Penland, S. Mizushima, C. Curran and J. V. Quagliano, *J. Am. Chem. Soc*., 1957, **79**, 1575.
16 J. P. Barbier and R. Hugel, *Inorg. Chim. Acta*, 1974, **10**, 93.
17 E. Giesbrecht and M. Kawashita, *J. Inorg. Nucl. Chem*., 1970, **32**, 2461.
18 L. G. Sillén and A. E. Martell, *Stability Constants of Metal-ion Complexes*, Chemical Society Special Publications 17 and 25 (Suppl. 1), The Chemical Society, London, 1964 and 1971.
19 J. Burgess, *Metal Ions in Solution*, Ellis Horwood Ltd, Chichester, 1978.
20 F. W. Miller, Jr. and H. R. Dittmar, *J. Am. Chem. Soc*., 1934, **56**, 848.
21 R. T. Conley, in *Infrared spectroscopy*, Allyn and Bacon Inc., 2nd edn., 1972, pp. 167–168.
22 R. Aumont, F. Genet, M. Passaret and Y. Toudic, *C. R. Acad. Sci. Paris, Ser. C*, 1971, **272**, 314.
23 M. Jansen, B. Klinkert and S. Elschner, *Mater. Res. Bull*., 1990, **25**, 1415.
24 J. B. Goodenough and J. M. Longo, *Landolt-Börnstein. Numerical Data and Functional Relationships in Science and Technology*, ed. K.-H. Hellwege and A. M. Hellwege, Springer-Verlag, Berlin, Heidelberg, New York, 1978, vol. 4a, p. 126.
25 H. D. Megaw, *Trans. Faraday Soc*., 1946, A42, 224.
26 Z. Jirák, S. Krupicka, Z. Simsa, M. Dlouha and S. Vratislav, *J. Magn. Magn. Mater*., 1985, **53**, 153.
27 H. M. Rietveld, *Acta Crystallogr*., 1967, **22**, 151.
28 H. M. Rietveld, *J. Appl. Crystallogr*., 1969, **2**, 65.
29 L. Lutterotti, P. Scardi and P. Maistrelli, *J. Appl. Crystallogr*., 1992, **25**, 459.
30 D. W. Marquardt, *J. Soc. Ind. Appl. Math*., 1963, **11**, 431.
31 G. Will, M. Bellotto, W. Parrish and M. Hart, *J. Appl. Crystallogr*., 1988, **21**, 182.
32 G. Caglioti, A. Paoletti and F. P. Ricci, *Nucl. Instrum. Methods*, 1958, **3**, 223.
33 P. Scardi, R. Di Maggio, L. Lutterotti and P. Maistrelli, *J. Am. Ceram. Soc*., 1992, **75**, 2828.
34 L. Lutterotti, P. Scardi and P. Maistrelli, *J. Appl. Crystallogr*., 1990, **23**, 246.
35 R. D. Shannon and C. T. Prewitt, *Acta Crystallogr*., 1969, **25**, 925.
36 K. Knízek, Z. Jirák, E. Pollert, F. Zounová and S. Vratislav, *J. Solid State Chem*., 1992, **100**, 292.
37 A. I. Vogel, *A Textbook of Quantitative Inorganic Analysis including Elementary Instrumental Analysis*, Longman, London, 4th edn., 1978.
38 H. P. Klug and L. P. Alexander, *X-Ray Diffraction Procedures for Polycrystalline and Amorphous Materials*, Wiley & Sons, New York, 2nd edn., 1974.
39 R. D. Sánchez, J. Rivas, D. Caeiro, M. Östlund, M. Servin, C. Vázquez-Vázquez, M. A. López-Quintela, M. T. Causa and S. B. Oseroff, *Mater. Sci. Forum*, 1997, **235–238**, 831.
40 R. D. Sánchez, J. Rivas, C. Vázquez-Vázquez, A. López-Quintela, M. T. Causa, M. Tovar and S. Oseroff, *Appl. Phys. Lett*., 1996, **68**, 134.

Paper 7/07226K; *Received* 6*th October*, 1997